







Article

Effect of Equal Channel Angular Extrusion on the Thermal Conductivity of an AX52 Magnesium Alloy

Zuzanka Trojanová ¹, Kristýna Halmešová ^{2,*}, Ján Džugan ², Zdeněk Drozd ¹,
Peter Minárik ¹ and Pavel Lukáč ¹

¹ Charles University, Faculty of Mathematics and Physics, Ke Karlovu 3, 121 16 Praha 2, Czech Republic; ztrojan@met.mff.cuni.cz (Z.T.); zdenek.drozd@mff.cuni.cz (Z.D.); peter.minarik@mff.cuni.cz (P.M.); pavel.lukac@mff.cuni.cz (P.L.)

² COMTES FHT, Průmyslová 995, 334 41 Dobřany, Czech Republic; jan.dzugan@comtesfht.cz

* Correspondence: kristyna.halmesova@comtesfht.cz; Tel.: +420-377-197-371

Received: 14 May 2020; Accepted: 5 June 2020; Published: 9 June 2020



Abstract: An AX52 magnesium alloy (nominal composition Mg-5Al-2Ca in w.%) was submitted to equal channel angular pressing (ECAP) using processing route A; 1–8 passes through the ECAP tool were applied. The thermal conductivity of the ECAP samples was measured using a flash method in the temperature interval from room temperature up to 350 °C. The microstructure and texture of the samples were studied by light and electron microscopy. The severe plastic deformation, realized by the ECAP, influences the thermal properties of the alloy. The possible microstructural parameters determining the thermal conductivity were analyzed. New dislocations, the grain, phase boundaries, and texture of the samples may perceptibly change the thermal properties.

Keywords: magnesium alloy; thermal diffusivity; thermal conductivity; thermal expansion; equal channel angular pressing; texture

1. Introduction

Severe plastic deformation has a significant influence on a variety of physical properties of processed magnesium materials. Besides the mechanical strength and deformability, which are primarily influenced by the grain refinement and texture formation [1], other physical properties such as the thermal conductivity [2], thermal expansion [3], or internal friction [4] are significantly affected as well.

The thermal properties of the processed materials are of high interest, especially because of the potential applications of magnesium-based components in various industrial branches where thermal management is needed. The efficiency of a thermal management system can be considered to be a measure of how effectively the system is capable of dissipating the heat which is generated in some points/areas. Today, research interest is focused primarily on high-power applications, including battery pack cooling and inverter equipment being used in the latest hybrid and all-electric vehicles. Magnesium has a high potential to be used in such applications because of its lightweight and heat dissipation properties in electronic parts, and vehicles play an important role in the utilization of Mg-based components [5–7].

The thermal conductivity of alloys is, in general, influenced by the alloying elements, thermal history, microstructure, and substructure [6,8–15]. In addition, the magnitude of the effect of these factors on the thermal conductivity may vary at different temperatures. Ying et al. showed that the thermal conductivity of pure Mg and Mg + 0.5 at%Al decreases with an increasing temperature, while the thermal conductivity of alloys with a higher Al content is independent to the temperature or increases with an increasing temperature [6]. A similar behavior was also found for Mg-Zn alloys [5].

The thermal conductivity increased in the temperature interval from 303 to 513 K for Mg + 1wt% Zn. Lee et al. measured the thermal conductivity in the AZ31 alloy prepared by twin roll casting [15], and they showed that the thermal conductivity increases in the temperature interval from $-125\text{ }^{\circ}\text{C}$ up to $400\text{ }^{\circ}\text{C}$.

The Mg-Al-Ca (AX) alloys were developed as creep resistant alloys for applications at elevated temperatures and, therefore, they may also be a good choice for heat-management systems. The utilization of Ca was supposed to be a cheaper variant to rare earth elements, which were usually used for high-temperature applications [16–23]. Good high-temperature properties are achieved because of the thermally stable second phases, and Ca also has a beneficial effect on the grain refinement, as was observed by several authors [24,25]. The phase selection and, consequently, the microstructure highly depend on the Ca/Al mass ratio. If the Ca/Al ratio is below 0.8, the formation of $\text{Mg}_{17}\text{Al}_{12}$ with a low eutectic temperature of $437\text{ }^{\circ}\text{C}$ is suppressed and the good mechanical properties at elevated temperatures may be ascribed to the $(\text{Mg},\text{Al})_2\text{Ca}$ particles with an eutectic temperature of $517\text{ }^{\circ}\text{C}$ and a melting point of $710\text{ }^{\circ}\text{C}$ [18,26–28]. Recently, Elamami et al. studied the microstructure and phase selection in Mg-Al-Ca-Mn cast alloys with a Ca/Al ratio in the range of 0.58–0.91 [29]. The detailed analysis showed that the Mg-Al-Ca alloys contain various second phases of Laves type, depending on the Ca/Al ratio and thermal treatment [29]. A higher ratio, $\text{Ca/Al} > 0.8$, leads to a complex microstructure with various Laves phases from C15 + C36 to C14 + C36 [20]. Therefore, the variation of the Ca/Al ratio is an effective tool to control the formation of various Laves phases and, consequently, to control the mechanical and creep properties of the material [29].

Special attention was, in the last few years, paid to the mechanical properties of magnesium materials submitted to severe plastic deformation (SPD). Trojanová et al., studying an AZ31 magnesium alloy submitted to accumulative roll bonding, showed that the SPD influences not only the mechanical properties, but also the thermal properties [2]. They found an increase in the thermal conductivity with the temperature and with the increasing number of passes through the rolling mill. While the microstructure and mechanical properties of cast and thermally treated AX alloys are reported in many papers, the properties of AX alloys submitted to SPD have only been studied rarely [1,30–33]. However, it was shown that the thermal stability of a fine-grained AX41 alloy is much better than that of the AZ31 alloy thanks to the thermally stable secondary phases [34]. Therefore, fine-grained AX alloys may be of high interest for heat management systems development.

In this study, the thermal conductivities of an Mg–Al–Ca alloys, submitted to equal channel angular pressing (ECAP) of up to eight passes were measured, and the microstructure of the ECAP samples was analyzed with the aim of explaining the corresponding conductivity variations depending on the number of ECAP passes. The interrelation of the microstructure and thermal behavior is subsequently discussed.

2. Materials and Methods

The AX52 magnesium alloy (nominal composition 5wt.% Al, 2wt.%Ca, balance Mg) was prepared with squeeze cast technology. Billets with dimensions of $10 \times 10 \times 100\text{ mm}^3$ were cut from castings and submitted to annealing at $390\text{ }^{\circ}\text{C}$ for 22 h. These semi-finished products were pressed through a rectangular channel of $10 \times 10\text{ mm}^2$ (inner angle $\Phi = 90^{\circ}$ outer curvature $\Psi = 0^{\circ}$) at the temperature of $250\text{ }^{\circ}\text{C}$ and using a cross-head speed of 10 mm/min . The material was subjected to 1, 2, 4, and 8 passes through the ECAP tool and the samples are hereafter depicted as 1P, 2P, 4P, and 8P, respectively. According to the literature data, route A was chosen [30].

The microstructure and substructure features of the samples were characterized by a ZEISS light microscope and a ZEISS Auriga Compact scanning electron microscope (SEM)(Carl Zeiss, Jena, Germany) equipped with an EDAX electron back-scatter diffraction (EBSD) system. The samples for all the measurements were polished to a mirror-like quality using a diamond suspension of grade 3, 1, and $0.25\text{ }\mu\text{m}$ and an alumina suspension of grade $0.05\text{ }\mu\text{m}$. Finally, the sample's surface was ion-polished by a Leica EM RES102 device in order to get a high-quality surface for the EBSD measurements.

The EBSD step size varied and depended on the analyzed scan size. It was selected to be 0.3 μm , 0.2 μm , 0.1 μm , and 0.1 μm for the 1P, 2P, 4P, and 8P samples, respectively. The samples intended for the light microscope were ground, polished, and finally etched for 2 s using an etchant for revealing the grain boundaries (20 ml of acetic acid, 3 g of picric acid, 20 ml of H_2O_3 , and 50 ml of ethanol, 95%).

Cylindrical samples for the thermal expansion measurements with a diameter of 4 mm and a length of 20 mm were machined from the processed parallelepipeds so that the cylinder axis was parallel to the processing direction (see Figure 1). The thermal expansion measurement was performed with an L75 PT-1600 (Linseis Messgeraete GmbH, Selb, Germany) push-rod dilatometer from room temperature to 350 $^\circ\text{C}$. The elongation of the samples, varying with the temperature, was measured in a protective atmosphere (argon in this case) by the LVDT sensor connected to the quartz push rods. The dilatometer system had a horizontal arrangement with two quartz push rods.

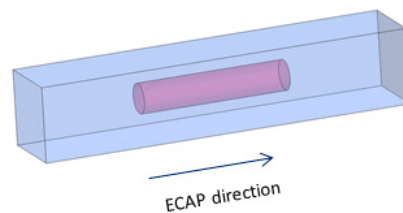


Figure 1. The orientation of the sample for the thermal expansion coefficient (CTE) measurements against the processing direction. ECAP: equal channel angular pressing.

The influences of the thermal expansion of the instrument's parts on the thermal expansion measurement were subtracted based on the correction measurement, where Al_2O_3 dummies were used as the reference specimens. The heating/cooling rate of the specimens was 1 $^\circ\text{C}/\text{min}$.

An LFA 1000 (Linseis, Germany) laser flash device with a vertical measurement set up was used for the determination of the specific heat and thermal diffusivity of the sample from room temperature to 350 $^\circ\text{C}$. The samples for the thermal measurements were cut from the cylinders depicted in Figure 1. A coin-shaped specimen, 12.7 mm in diameter and 2 mm in thickness, was irradiated from one side by a short laser pulse, and the rise of the temperature was measured on the opposite side by an infrared sensor. Four specimens were measured at once and measurements were repeated three times. Then, the mean value and standard deviation were calculated. The thermal diffusivity coefficient corresponds to the half-time of the temperature increase according to the formula:

$$a = 0.1388\ell^2/t_{0.5}, \quad (1)$$

where ℓ is the sample thickness and $t_{0.5}$ is the time at 50% of the temperature increase.

The specific heat coefficient c_p corresponds to the total temperature increase according to the relationship: $c_p = c_{pr}(\Delta T_r/\Delta T)(m_r/m)$, where c_p , c_{pr} are the specific heats of the sample and reference sample, respectively; ΔT , ΔT_r are temperature increases after the laser pulse; m , m_r are their masses. As a reference, a molybdenum sample was applied. The room temperature density of the samples was estimated by hydrostatic weighing at room temperature.

3. Results

3.1. Microstructure of the Samples

The light micrograph of the as-cast sample microstructure is shown in Figure 2. The α -Mg grains and continuous network of the intermetallic compounds in the dendritic structure (due to the low solubility of the Ca in the α -Mg-Al solid solution) are typical features of the microstructure. The chemical analysis showed that the second phase particles are Al_2Ca eutectics. The dendritic branches were broken during the squeeze cast process, as can be seen in the SEM micrograph presented in Figure 3.

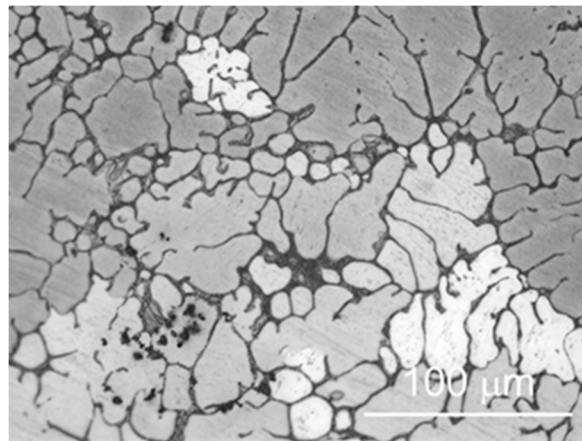


Figure 2. The light micrograph of the as-cast condition.

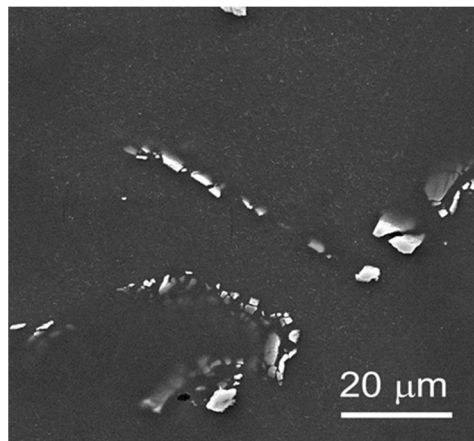
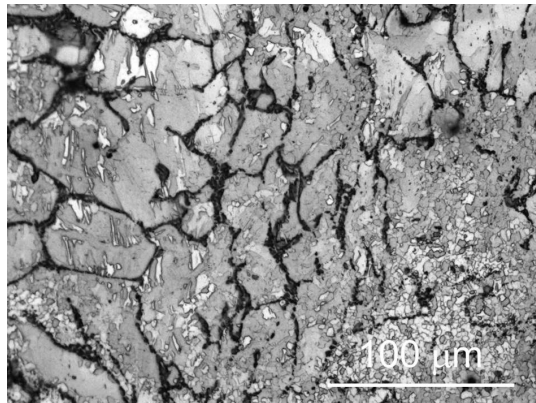


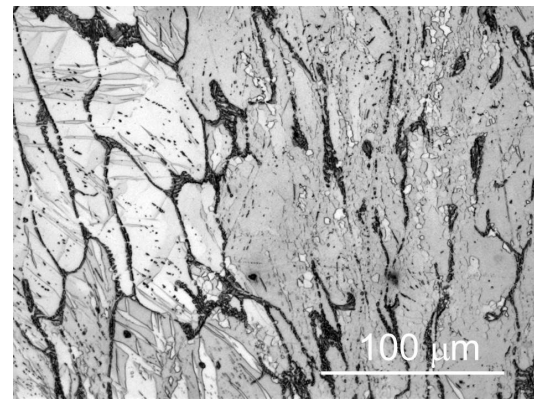
Figure 3. The SEM micrograph of the broken particles in the dendritic branches.

The light micrographs of the samples processed by 1, 2, 4, and 8 ECAP passes are shown in Figure 4a–h. The micrographs in the left column were taken from the perpendicular section (P) to the processing direction, while the micrographs in the right column were taken from the longitudinal (L) section. The microstructure was highly inhomogeneous after the first pass; new small grains were formed inside the former ones. After two passes, the bimodal grain size distribution was formed due to the partial recrystallization. Distinctive twins appeared in the coarser grains in both the 1P and 2P samples (Figure 4b: 1P_L, 4d: 2P_L). The second phase of the net-like distribution was partially disintegrated. A high area fraction of small grains was observed after four passes (Figure 4e,f) and the continuous network of the second phase particles was destroyed; the disintegrated particles were arranged in rows oriented along the processing direction. After eight passes (Figure 4g,h), the grain structure was nearly uniform and the tiny second phase particles were arranged in rows parallel to the processing direction. The scanning electron micrograph (SEM) images presented in Figure 5a,b showed that the morphology of the second phase after eight passes through the ECAP changed. The amount of the Al_2Ca phase was not affected by the processing, because its amount was set by the phase diagram. A high degree of fragmentation and some degree of spheroidization did occur, but the secondary phase did not dissolve into the matrix at the temperature used for the processing. The initial size of the particles was up to 10 μm , which is shown in Figure 3, and their distribution is highly limited to the dendritic branches, as shown in Figure 2. The processing obviously led to a decrease in the particle size, as shown in Figure 5. The size of the particles became much smaller ($\sim 1 \mu\text{m}$). This can be primarily attributed to the high magnitude of the shear deformation acting during the ECAP process.

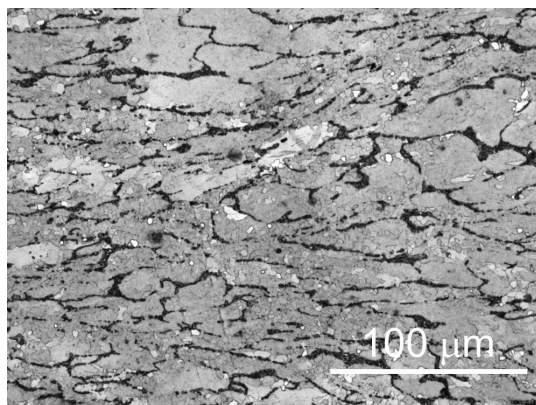
However, the particles were not sharp, therefore, some degree of a thermal effect was considered. A similar behavior, i.e., the spheroidization of the eutectic phase in the Mg-Al-Ca alloys during the ECAP process, was also observed by other authors [35]. The pores visible in Figure 5a,b are holes corresponding to the particles that fell off during the metallographic preparation of the samples.



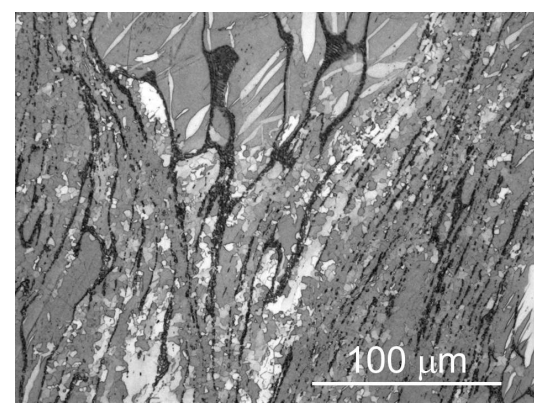
a) 1P_P



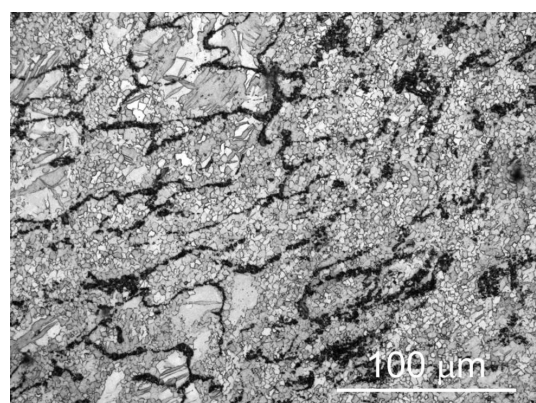
b) 1P_L



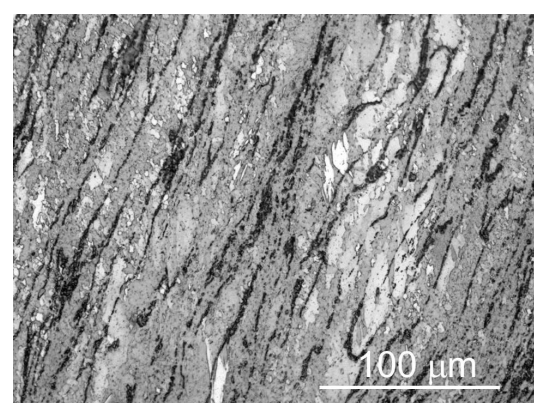
c) 2P_P



d) 2P_L



e) 4P_P



f) 4P_L

Figure 4. Cont.

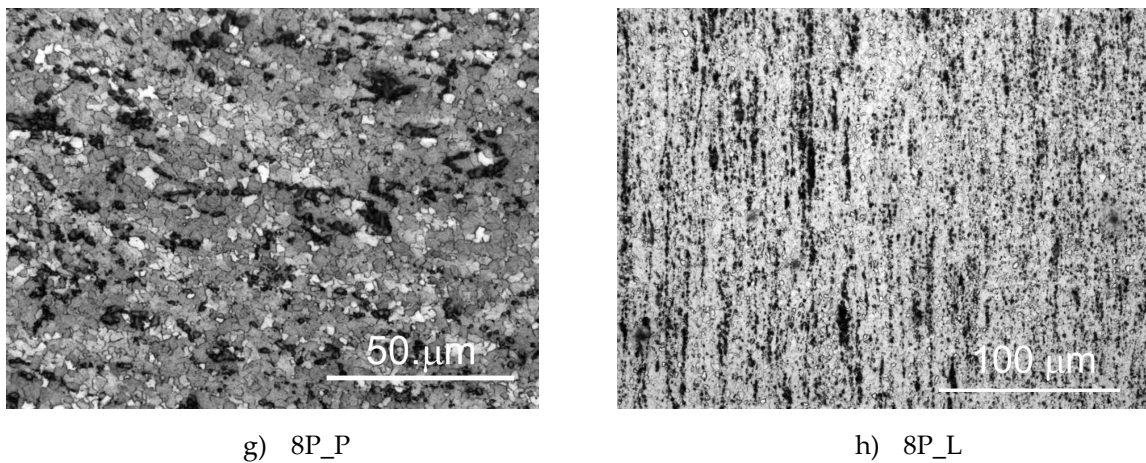


Figure 4. The light micrographs of the samples processed by ECAP (a,b; c,d; e,f; and g,h for samples after 1, 2, 4, and 8 passes, respectively). The P and L micrographs were taken from the perpendicular and the longitudinal sections to the processing direction, respectively.

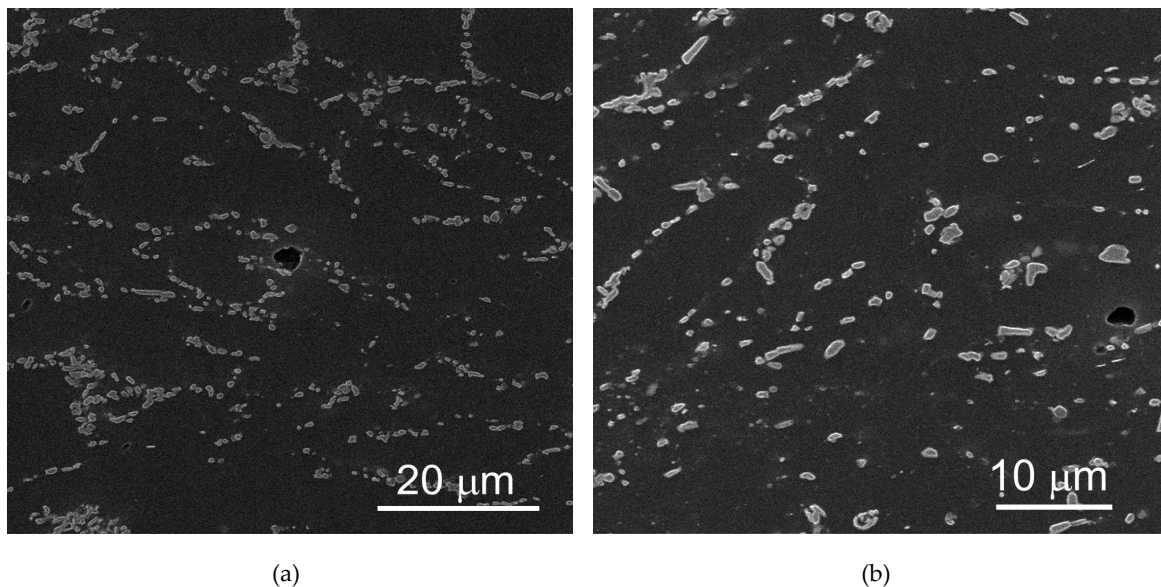


Figure 5. The SEM micrographs taken after 8 passes from (a) the perpendicular section and (b) the longitudinal section to the processing direction.

Figure 6 shows the EBSD orientation maps measured in the perpendicular section to the processing direction. The observed microstructural evolution corresponds to the evolution described above by the light microscopy. The major benefit of the EBSD measurement is the possibility to statistically calculate the grain size and to qualitatively observe the residual strain. The large grains present in the samples processed by one and two ECAP passes exhibit a high degree of color variation corresponding to a large amount of residual strain. Note that the recrystallization occurred not only along the former grain boundaries, but also inside the grains, where the deformation was high enough for the onset of the recrystallization even after the first pass. Such a microstructural development is often observed in deformed alloys which exhibit a high amount of second phase particles [35,36]. Second phase particles may act as strain concentrators and help the recrystallization. After four and eight passes, the microstructure becomes almost uniform with a high area fraction of fine grains. The average grain size was calculated as a weighted average with the area fraction as the weight, which was $\sim 4 \mu\text{m}$ in both samples.

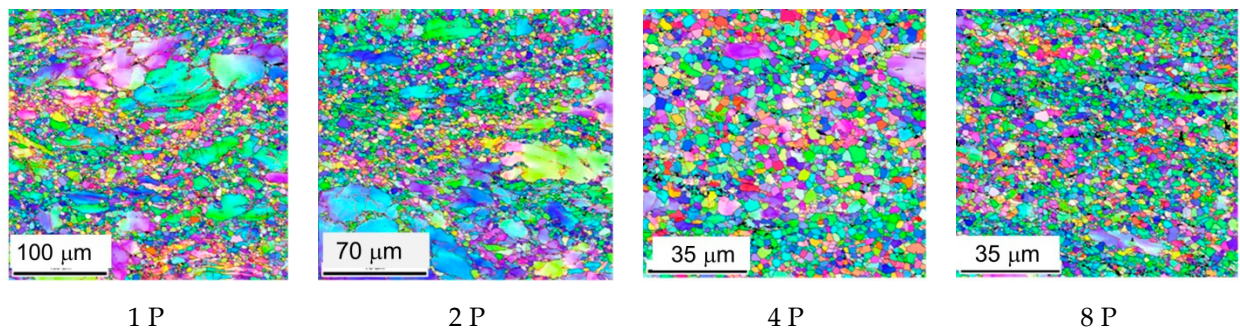


Figure 6. The electron back-scatter diffraction (EBSD) inverse pole figures of the ECAP extruded samples.

A rapid decrease in the grain size was achieved between the as-cast sample and the sample after the first pass and between the second and fourth ECAP passes. The mean grain size values taken from the perpendicular section are reported in Table 1.

Table 1. Grain size in samples.

Number of passes	0	1	2	4	8
Grain size (μm)	63	28	21	4	3.4

3.2. Texture of Samples

The cast alloy was considered to be texture-free and, therefore, the texture characterization was not performed. On the other hand, ECAP is known to cause strong texture formation. Figure 7 shows the EBSD pole figures calculated from the meaningfully large EBSD maps comprising a high number of grains. The results show that the texture formation was typical for ECAP route type A with only one texture element representing the grains with basal planes parallel to the processing direction and perpendicular to the feed-in direction denoted as Z [1]. This texture element was formed by the extensive activation of the twinning in the feed-in channel and the subsequent activation of the primarily $\langle c + a \rangle$ when the material passed through the sharp angle. This texture development is shown and discussed in detail elsewhere [1].

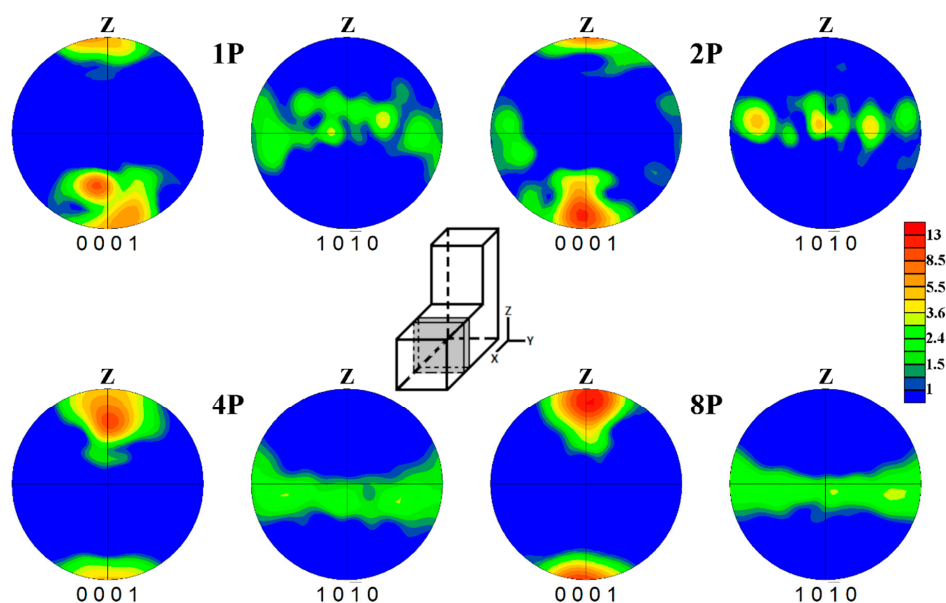


Figure 7. The pole figures of ECAP extruded samples.

3.3. Thermal Properties

The thermal diffusivity, a , together with the values of the specific heat, c_p , measured at the different temperatures for the samples submitted to various numbers of passes, and the corresponding results are reported in Table 2. Two results are of note: (i) the diffusivity values decreased with increasing temperature for all the samples and (ii) there was no monotonous tendency observed on the number of passes for a given temperature.

Table 2. The thermal diffusivity, a , and the specific heat, c_p , depending on the temperature T and number of passes (0–8 P).

No. of Passes	0 P		1 P		2 P		4 P		8 P	
T °C	a cm ² s ⁻¹	c_p J kg ⁻¹ K ⁻¹	a cm ² s ⁻¹	c_p J kg ⁻¹ K ⁻¹	a cm ² s ⁻¹	c_p J kg ⁻¹ K ⁻¹	a cm ² s ⁻¹	c_p J kg ⁻¹ K ⁻¹	a cm ² s ⁻¹	c_p J kg ⁻¹ K ⁻¹
20	0.42	950	0.44	1122	0.40	1153	0.41	1060	0.45	990
50	0.41	963	0.42	1112	0.38	1215	0.39	1140	0.44	973
100	0.39	1027	0.40	1277	0.35	1205	0.36	1137	0.41	1015
150	0.37	1042	0.39	1273	0.33	1254	0.34	1136	0.39	1067
200	0.37	1111	0.38	1339	0.32	1282	0.33	1185	0.39	1056
250	0.35	1131	0.37	1327	0.31	1308	0.31	1185	0.38	1122
300	0.34	1108	0.36	1403	0.30	1302	0.31	1214	0.36	1154

The thermal conductivity κ (W m⁻¹ K⁻¹) is a product of three quantities

$$\kappa = a\rho c_p, \quad (2)$$

where a is the thermal diffusivity (cm² s⁻¹), ρ is the density (kg m⁻³), and c_p is the specific heat capacity (J kg⁻¹ K⁻¹) at a constant pressure. The experimental values of the thermal diffusivity, a , and the specific heat, c_p , used for the calculation are stated in Table 2. Considering relationship (1), the thermal expansivity of the samples thickness

$$\ell = \ell_{20} [1 + \alpha(T - 20)] \quad (3)$$

and temperature dependence of the density can be expressed using the thermal expansion coefficient

$$\rho = \rho_{20} / [1 + \alpha(T - 20)]^3, \quad (4)$$

Here, ℓ_{20} and ρ_{20} are the sample thickness and density at 20 °C, respectively. The thermal conductivity can be expressed in accordance with the formula:

$$\kappa = \frac{0.1388\ell_{20}^2}{t_{0.5}(T)} \rho_{20} c_p(T) / [1 + (T - 20)] \quad (5)$$

The calculated values of the thermal conductivity are reported in Table 3; for the calculations, the thermal expansion coefficient, α , the values introduced in Table 3 were also used.

Table 3. The thermal expansion coefficient, α , and the thermal conductivity, κ , depending on the temperature T and number of passes (0–8 P).

No. of Passes	0 P		1 P		2 P		4 P		8 P		
	T °C	$\alpha \times 10^{-6}$ K ⁻¹	κ W m ⁻¹ K ⁻¹	T °C	$\alpha \times 10^{-6}$ K ⁻¹	κ W m ⁻¹ K ⁻¹	T °C	$\alpha \times 10^{-6}$ K ⁻¹	κ W m ⁻¹ K ⁻¹	T °C	$\alpha \times 10^{-6}$ K ⁻¹
20	24.96	70.2	25.42	87.0	24.81	79.1	25.66	73.9	25.08	75.5	75.5
50	25.36	69.4	25.89	82.3	25.30	79.0	26.07	75.5	25.42	72.5	72.5
100	26.02	70.3	26.67	89.9	26.11	71.9	26.75	69.2	25.98	70.4	70.4
150	26.68	67.6	27.45	87.2	26.91	70.3	27.44	65.0	26.53	70.3	70.3
200	27.33	72.0	28.23	89.3	27.72	69.4	28.12	65.6	27.09	69.5	69.5
250	27.99	69.3	29.02	86.0	28.53	68.3	28.80	61.3	27.65	71.8	71.8
300	28.65	65.8	29.80	88.4	29.34	65.5	29.48	62.6	28.21	69.9	69.9

4. Discussion

The ECAP processing is usually performed at elevated temperature (250 °C, especially in the case of magnesium), therefore, dynamic recrystallization (DRX) is considered as the dominant refinement mechanism. New small grains predominantly decorate the bigger ones, but as shown in Figures 4a–d and 6, the formation of small grains in the middle of the large grains after the first and second ECAP steps was observed as well. This effect is primarily associated with the presence of the second phase particles [35,36]. The grain structure was subsequently refined and homogenized with an increasing number of ECAP passes until the whole microstructure was fine-grained and uniform. The grain refinement by ECAP and the features of the DRX in the Mg–Al alloys containing Ca were already studied by several authors [37–39], therefore, it is not the primary focus of this study. It was shown that particles containing Ca stimulate the nucleation and effectively pin the deformation-induced high angle grain boundaries (HAGBs). In addition, the Ca additives also suppress the twinning [39,40].

As mentioned above, the notable color variation present in the bigger grains (see Figure 6 1P and 2P) indicates significant internal stress. These stresses are predominantly formed at the interface between the hard (Mg,Al)₂Ca eutectics and the magnesium matrix due to the generation and movement of the dislocations and their pile up in the vicinity of the incompatible phase boundaries. In two-phase materials, large strain gradients are induced in the matrix, and geometrically necessary dislocations are generated in order to accommodate these gradients and, thus, allow the matrix to deform in a compatible way. The total dislocation density, ρ_t , generated in the material can be written as a sum of the geometrically necessary dislocations, ρ_G , and the dislocations that are generated in the matrix, ρ_s .

$$\rho_t = \rho_G + \rho_s. \quad (6)$$

These dislocations are partially lost during the recovery and recrystallization processes. The recrystallization originates at the deformation zones as is obvious from Figure 6 1P and 2P, where the newly created dislocations are consumed.

According to Fourier's law of thermal conductivity, the local heat flux density, q , is regarded as

$$q = \kappa \text{grad } T, \quad (7)$$

where the thermal conductivity, κ , may be the sum of two components

$$\kappa = \kappa_{ph} + \kappa_e, \quad (8)$$

reflecting two independent carriers: phonons and electrons.

The maximum in the phonon part, κ_{ph} , is about $0.1\theta_D$ at low temperatures and θ_D is the Debye temperature of a material ($\theta_D(\text{Mg}) = 318 \text{ K}$) [41]. The thermal conductivity at a certain temperature of a reasonable pure metal is proportional to the electrical conductivity, σ , as is expressed in the Wiedemann–Franz law

$$\kappa = \sigma LT, \quad (9)$$

where the constant L is the Lorenz number. Note that the Wiedemann–Franz law strictly compares the electronic thermal conductivity with the electrical conductivity. In alloys, the overall thermal conductivity may contain a significant contribution from phonons. Considering ℓ_e , the mean free path of the electrons, n , the number of electrons per unit volume, and \bar{v} , their mean velocity, the thermal conductivity of the electrons is

$$\kappa_e = \frac{nk_B\ell_e\bar{v}}{2}, \quad (10)$$

where k_B is the Boltzmann constant. In real metals, the mean free path of the electrons may be restricted by some scatter process on the lattice defects, lattice phonons, and collisions with each other.

The thermal conductivity of alloys can be described with the Smith–Palmer relationship [42]

$$\kappa = C \frac{LT}{\rho} + D, \quad (11)$$

where C and D are constants and ρ is the electrical resistance. The Smith–Palmer equation assumes temperature independent phonon thermal conductivity via the constant D . The equation is suited to a situation where point defects interact with the phonons and electrons.

The thermal conductivity extrapolated to room temperature depending on the number of ECAP passes is shown in Figure 8a. The conductivity maximum was observed after the first ECAP pass, then the conductivity rapidly decreased. A small increase in the conductivity after the eighth pass was found. Generally, the thermal conductivity of magnesium alloys may depend on their composition, temperature, and thermomechanical treatment. The thermal conductivity may be affected by various microstructural factors such as the texture, grain size, precipitates, and dislocations [43]. In the ECAP AX52 alloy, all these influences may play a role; the microstructure and substructure of the samples were changed after the passes through the ECAP tool. The temperature dependencies of the thermal conductivity measured for the samples in the as-cast state and after the first and eighth passes are reported in Figure 8b. For clarity purposes only, straight lines are shown in Figure 8b, the dependences estimated for the other passes lie among them. As it can be easily seen, the temperature dependence of the thermal conductivity is linear, which complies with the Smith–Palmer equation.

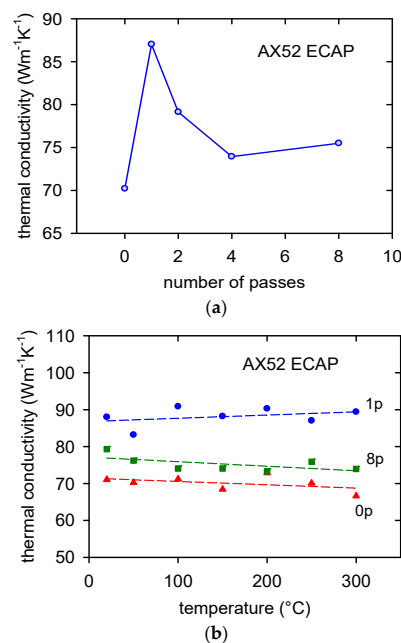


Figure 8. The thermal conductivity, κ , depending on (a) the number of passes and (b) the temperature.

The temperature dependence of the thermal conductivity was weak. This result is different from the results of other authors who measured the extremely sensitive behavior [2,44,45]. Zhong et al. studied the microstructure and thermal conductivity of an extruded ZM60 magnesium alloy in the as-received state and after the pre-strain in compression [45]. They estimated an increase in the thermal conductivity after the pre-deformation of up to 8.3%. A further deformation up to 10.5% led to a decrease in the thermal conductivity. The measured conductivity increase was explained by the twin formation and the changes in the texture. They ascribed this increase to an increase in the mean free path of the electrons and phonons in the *c*-axis direction of the grains. Similarly, Bass [46] pointed out that the electrical conductivity of a magnesium single crystal along the $\langle c \rangle$ axis is higher than that in the $\langle a \rangle$ direction, i.e., we can also expect $\kappa(c)/\kappa(a) > 1$ for the thermal conductivity. The ECAP process in the AX52 samples oriented the basal planes in the samples to be parallel to the channel walls. The conductivity was measured in the processing direction, i.e., in the basal plane, where due to the anisotropy of the hexagonal magnesium cell, the values should be lower compared with those in the perpendicular direction. Texture strengthening with an increasing number of ECAP passes should, therefore, cause a decrease in the conductivity. This dependence was observed. Besides this texture effect, it is necessary to consider the influence of the dislocations on both the electron and lattice conductivity. According to Schockley [47], dislocations limit the thermal (and also the electrical) conductivity due to the electron scattering on the dislocation lines existing in a crystal, which may bond the conduction electrons and, thereby, decrease the conductivity. With an increasing number of passes, the grain size was reduced. On the other hand, the area of the grain boundaries was substantially enlarged and, therefore, so too was the area of new interfaces and sites for electron and phonon scattering [48]. However, the existing continuous eutectic phases present in the as-cast sample impede the electron transportation. The observed fragmentation of these phases during the ECAP pressing may improve the thermal/electrical conductivity and it is the very probable reason for the significant conductivity increase after the first pass.

5. Conclusions

In summary, the AX52 magnesium alloy was submitted to ECAP processing. The microstructural observations together with the thermal conductivity measurements allow us to conclude:

1. The microstructure was substantially refined by equal channel angular (ECA) pressing performed via route A. The grain size decreased after eight passes from 63 to 3.4 μm .
2. The pronounced texture was formed during the ECAP processing, where the basal planes were primarily oriented parallel to the processing direction.
3. The thermal conductivity was perceptibly influenced by severe plastic deformation. The thermal conductivity, estimated at room temperature, increased after the first ECAP pass and then decreased after the subsequent passes.
4. The temperature dependence of the thermal conductivity was only weak.
5. The influence of the structural parameters on the thermal conductivity is a complex problem, where the conductivity is a result of the interplay of various electron and phonon scattering processes.

Author Contributions: Z.T. conceived and designed the experiments; K.H. and J.D. performed the thermal experiments; P.M. dealt with the microstructure and texture of the alloys; Z.T. and Z.D. analyzed the data; Z.T., P.M., and P.L. wrote the paper. All authors have read and agreed to the published version of the manuscript.

Funding: K.H., and J.D. acknowledge the partial financial support by the Ministry of Trade and Industry of the Czech Republic within the frame of institutional funding of the long-term development of research organizations. P.M. acknowledges the partial financial support by ERDF under project No. CZ.02.1.01/0.0/0.0/15 003/0000485.

Acknowledgments: The authors thank Peter Palček for the provision of electron micrographs 5a,b.

Conflicts of Interest: The authors declare no conflicts of interest.

References

1. Krajňák, T.; Minárik, P.; Stráská, J.; Gubicza, J.; Máthis, K.; Janeček, M. Influence of equal channel angular pressing on texture, microstructure and mechanical properties of extruded AX41 magnesium. *J. Alloys Compd.* **2017**, *705*, 273–282. [[CrossRef](#)]
2. Trojanová, Z.; Halmešová, K.; Drozd, Z.; Šíma, V.; Lukáč, P.; Džugan, J.; Minárik, P. Thermal conductivity of an AZ31 sheet after accumulative roll bonding. *Crystals* **2018**, *8*, 278. [[CrossRef](#)]
3. Drozd, Z.; Trojanová, Z.; Halmešová, K.; Džugan, J.; Lukáč, P.; Minárik, P. Anisotropy of Thermal Expansion in an AZ31 Magnesium Alloy Subjected to the Accumulative Roll Bonding. *Acta Phys. Pol. A* **2018**, *134*, 820–823. [[CrossRef](#)]
4. Trojanová, Z.; Drozd, Z.; Lukáč, P.; Minárik, P.; Džugan, J.; Halmešová, K. Amplitude-dependent internal friction in AZ31 alloy sheets submitted to accumulative roll bonding. *Low Temp. Phys. Fiz. Nizk. Temp.* **2018**, *44*, 966–972. [[CrossRef](#)]
5. Ying, T.; Zheng, M.Y.; Li, Z.T.; Qiao, X.G.; Xu, S.W. Thermal conductivity of as-cast and as-extruded binary Mg–Zn alloys. *J. Alloys Compd.* **2015**, *621*, 250–255. [[CrossRef](#)]
6. Ying, T.; Zheng, M.Y.; Li, Z.T.; Qiao, X.G. Thermal conductivity of as cast and as extruded binary Mg–Al alloys. *J. Alloys Compd.* **2014**, *608*, 19–24. [[CrossRef](#)]
7. Liu, Y.F.; Jia, X.J.; Qiao, X.G.; Xu, S.W.; Zheng, M.Y. Effect of La content on Microstructure, thermal conductivity and mechanical properties of Mg–4Al magnesium alloys. *J. Alloys Compd.* **2019**, *806*, 71–78. [[CrossRef](#)]
8. Wang, C.; Cui, Z.; Liu, H.; Chen, Y.; Ding, W.; Xiao, S. Electrical and thermal conductivity in Mg–5Sn alloy at different aging status. *Mater. Des.* **2015**, *84*, 48–52. [[CrossRef](#)]
9. Pan, H.; Pan, F.; Yang, R.; Peng, J.; Tang, A.; Huang, Q.; Song, K.; Gao, Z. Thermal and electrical conductivity of Mg–Zn–Al alloys. *Mater. Sci. Technol.* **2014**, *30*, 988–994. [[CrossRef](#)]
10. Oh, G.Y.; Jung, Y.G.; Yang, W.; Kim, S.K.; Lim, H.K.; Kim, Y.J. Investigation of thermal conductivity and mechanical properties of Mg–4Zn–0.5Ca–xY alloys. *Mater. Trans.* **2015**, *56*, 1887–1892. [[CrossRef](#)]
11. Rudajevová, A.; Staněk, M.; Lukáč, P. Determination of thermal diffusivity and thermal conductivity of Mg–Al alloys. *Mater. Sci. Eng. A* **2003**, *341*, 152–157. [[CrossRef](#)]
12. Su, C.; Li, D.; Ying, T.; Zhou, L.; Li, L.; Zeng, X. Effect of Nd content and heat treatment on the thermal conductivity of Mg Nd alloys. *J. Alloys Compd.* **2015**, *685*, 114–121. [[CrossRef](#)]
13. Yamasaki, M.; Kawamura, Y. Thermal diffusivity and thermal conductivity of Mg–Zn–rare earth element alloys with long-period stacking ordered phase. *Scripta. Mater.* **2009**, *60*, 264–267. [[CrossRef](#)]
14. Rudajevová, A.; Lukáč, P. Comparison of the thermal properties of AM20 and AS21 magnesium alloys. *Mater. Sci. Eng. A* **2005**, *397*, 16–21. [[CrossRef](#)]
15. Lee, S.; Ham, H.J.; Kwon, S.Y.; Kim, S.W.; Suh, C.M. Thermal conductivity of magnesium alloys in the temperature range from –125 °C to 400 °C. *Int. J. Thermophys.* **2013**, *34*, 2343–2350. [[CrossRef](#)]
16. Perkguleryuz, M. *Magnesium Alloys and Their Applications*; Kainer, K.U., Ed.; Willey-VCH: Weinheim, Germany, 2003; pp. 65–85.
17. Ninomiya, R.; Ojio, T.; Kubota, K. Improved heat resistance of Mg–Al alloys by the Ca addition. *Acta Metall.* **1995**, *43*, 669–674. [[CrossRef](#)]
18. Gjestland, H.; Nussbaum, G.; Regazzoni, G.; Lohne, O.; Bauger, O. Stress-relaxation and creep behaviour of some rapidly solidified magnesium alloys. *Mater. Sci. Eng. A* **1991**, *134*, 1197–1200. [[CrossRef](#)]
19. Terada, Y.; Ishimatsu, N.; Sota, R.; Sato, T.; Otori, K. Creep Characteristics of Ca-Added Die-Cast AM50 Magnesium Alloys. *Mater. Sci. Forum* **2003**, *419*, 459–464. [[CrossRef](#)]
20. Wenwen, D.; Yangshan, S.; Xuegang, M.; Feng, X.; Min, Z.; Dengyun, W. Microstructure and mechanical properties of Mg–Al based alloy with calcium and rare earth additions. *Mater. Sci. Eng. A* **2003**, *356*, 1–7. [[CrossRef](#)]
21. Luo, A.A. Magnesium casting technology for structural applications. *J. Magnes. Alloys.* **2013**, *1*, 2–22. [[CrossRef](#)]
22. Pekguleryuz, M.; Celikin, M. Creep resistance in magnesium alloys. *Int. Mater. Rev.* **2010**, *55*, 197–217. [[CrossRef](#)]
23. Liu, M.; Wang, Q.; Liu, Z.; Wang, G.; Wu, G.; Zhu, Y.; Ding, W. Behavior of Mg–Al–Ca alloy during solution heat treatment at 415 °C. *J. Mater. Sci. Lett.* **2002**, *21*, 1281–1283. [[CrossRef](#)]

24. Jiang, B.; Liu, W.; Qiu, M.; Zhang, X.; Pan, F. Grain refinement of Ca addition in a twin-roll-cast Mg–3Al–1Zn alloy. *Mater. Chem. Phys.* **2012**, *133*, 611–616. [[CrossRef](#)]
25. Chen, Y.; Liu, H.; Ye, R.; Liu, G. Effects of the addition of Ca and Sb on the microstructure and mechanical properties of AZ91 magnesium. *Mater. Sci. Eng. A* **2013**, *587*, 262–267. [[CrossRef](#)]
26. Luo, A.A. Recent magnesium alloy development for elevated temperature applications. *Int. Mater. Rev.* **2004**, *49*, 13–30. [[CrossRef](#)]
27. Pekguleryuz, M.O.; Kaya, A.A. Creep Resistant Magnesium Alloys for Powertrain Applications. *Adv. Eng. Mater.* **2004**, *5*, 866–878. [[CrossRef](#)]
28. Luo, A.A.; Powell, B.R.; Sachdev, A.K. Computational phase equilibria and experimental investigation of magnesium–aluminum–calcium alloys. *Intermetallics* **2012**, *24*, 22–29. [[CrossRef](#)]
29. Elamami, H.A.; Incesu, A.; Korgiopoulus, K.; Pekguleryuz, M.; Gungor, A. Phase selection and mechanical properties of permanent-mold cast Mg–Al–Ca–Mn alloys and the role of Ca/Al ratio. *J. Alloys Compd.* **2018**, *764*, 216–225. [[CrossRef](#)]
30. Krajňák, T.; Minárik, P.; Gubicza, J.; Máthis, K.; Kužel, R.; Janeček, M. Influence of equal channel angular pressing routes on texture, microstructure and mechanical properties of extruded AX41 magnesium alloy. *Mater. Charact.* **2017**, *123*, 282–293. [[CrossRef](#)]
31. Trojanová, Z.; Halmešová, K.; Džugan, J.; Pačcek, P.; Minárik, P.; Lukáč, P. Influence of strain rate on deformation behaviour of an AX52 alloy processed by equal channel angular pressing (ECAP). *Lett. Mater.* **2018**, *8*, 517–523. [[CrossRef](#)]
32. Krajňák, T.; Minárik, P.; Stráský, J.; Máthis, K.; Janeček, M. Mechanical properties of ultrafine-grained AX41 magnesium alloy at room temperature and elevated temperatures. *Mater. Sci. Eng. A* **2018**, *731*, 438–445. [[CrossRef](#)]
33. Kim, J.W.; Lee, Y.G. High strength Mg–Al–Ca alloy with ultrafine grain size sensitive to strain rate. *Mater. Sci. Eng. A* **2011**, *528*, 2062–2066. [[CrossRef](#)]
34. Janeček, M.; Krajňák, T.; Minárik, P.; Čížek, J. Structural stability of ultra-fine grained magnesium alloys processed by equal channel angular pressing. *Mater. Sci. Eng.* **2017**, *194*, 012022. [[CrossRef](#)]
35. Wang, C.; Ma, A.; Sun, J.; Liu, H.; Huang, H.; Yang, Z. Effect of ECAP process on as-cast and as-homogenized Mg–Al–Ca–Mn alloys with different Mg₂Ca morphologies. *J. Alloys Compd.* **2019**, *793*, 259–270. [[CrossRef](#)]
36. Yang, Z.; Ma, A.; Liu, H.; Sun, J.; Song, D.; Wang, C.; Yuan, Y.; Jiang, J. Multimodal microstructure and mechanical properties of AZ91 Mg alloy prepared by equal channel angular pressing plus aging. *Metals* **2018**, *8*, 763. [[CrossRef](#)]
37. Masoudpanah, S.M.; Mahmudi, R. Effects of rare-earth elements and Ca additions on the microstructure and mechanical properties of AZ31 magnesium alloy processed by ECAP. *Mater. Sci. Eng. A* **2009**, *526*, 22–30. [[CrossRef](#)]
38. Hakamada, M.; Watazu, A.; Saito, N.; Iwasaki, H. Dynamic recrystallization during hot compression of as-cast and homogenized noncombustible Mg–9Al–1Zn–1Ca (in mass%) alloys. *Mater. Sci. Eng. A* **2010**, *527*, 7143–7146. [[CrossRef](#)]
39. Kaibyshev, R. Dynamic recrystallization in magnesium alloys. In *Advances in Wrought Magnesium Alloys*; Bettels, C., Barnett, M., Eds.; Woodhead Publishing Limited: Oxford, UK, 2012; pp. 186–225. [[CrossRef](#)]
40. Ion, S.E.; Humphreys, F.J.; White, H.S. Dynamic recrystallization and the development of microstructure during the high temperature deformation of magnesium. *Acta Metall.* **1982**, *30*, 1909–1919. [[CrossRef](#)]
41. Li, S.; Yang, X.; Hou, J.; Du, W. A review on thermal conductivity of magnesium and its alloys. *J. Magnes. Alloys* **2020**, *8*, 78–90. [[CrossRef](#)]
42. Uher, C. Thermal conductivity of metals. In *Thermal Conductivity*; Tritt, M., Ed.; Kuwen Academic/Plenum Publishers: New York, NY, USA, 2004. [[CrossRef](#)]
43. Lumley, R.N.; Polmear, I.J.; Groot, H.; Ferrier, J. Thermal characteristics of heat-treated aluminum high-pressure die-castings. *Scr. Mater.* **2008**, *58*, 1006–1009. [[CrossRef](#)]
44. Tong, X.; You, G.; Ding, Y.; Xue, H.; Wang, Y.; Guo, W. Effect of grain size on low-temperature electrical resistivity and thermal conductivity of pure magnesium. *Mater. Lett.* **2018**, *229*, 261–264. [[CrossRef](#)]
45. Zhong, L.; Wang, Y.; Luo, H.; Luo, C.; Peng, J. Evolution of the microstructure, texture and thermal conductivity of as-extruded ZM60 magnesium alloy in pre-compression. *J. Alloys Compd.* **2019**, *775*, 707–713. [[CrossRef](#)]
46. Bass, J.; Fisher, K.H. *Landolt-Börnstein database, New Series III/15a*; Springer: Berlin/Heidelberg, Germany, 1982.

47. Osip'yan, Y.A. Interaction of electrons with dislocations in crystals. *Her. Russ. Acad. Sci.* **2006**, *76*, 437–445. [[CrossRef](#)]
48. Fiks, V.B. Interaction of conduction electrons with single dislocation in metals. *Sov. Phys. JETP* **1981**, *53*, 1209–1211.



© 2020 by the authors. Licensee MDPI, Basel, Switzerland. This article is an open access article distributed under the terms and conditions of the Creative Commons Attribution (CC BY) license (<http://creativecommons.org/licenses/by/4.0/>).